

Turbulent entrainment in sediment-laden flows interacting with an obstacle

Richard I. Wilson,^{1,a)} Heide Friedrich,^{1,b)} and Craig Stevens^{2,c)}

¹Department of Civil and Environmental Engineering, University of Auckland, Auckland, New Zealand

²National Institute of Water and Atmospheric Research, Wellington, New Zealand and Department of Physics, University of Auckland, Auckland, New Zealand

(Received 8 August 2016; accepted 10 March 2017; published online 30 March 2017)

Temporal entrainment characteristics and mixing processes of sediment-laden turbidity currents interacting with a rectangular obstacle are investigated through lock-exchange experiments. Building on the Morton-Taylor-Turner hypothesis, dependency of temporal entrainment on non-dimensional parameters is examined. Currents of varying density are analyzed during the slumping phase over smooth and rough substrates. Quantitative and qualitative observations of the currents are captured through high resolution, high framerate binary thresholding techniques. Additionally, siphoning techniques are used to compare the density structure of the currents before and after the obstacle. Upon interaction with the obstacle, currents are found to experience four stages of entrainment: (i) lateral entrainment stage; (ii) jet stage; (iii) collapsing stage; (iv) re-establishment stage. The entrainment parameter was within the range of other studies for both obstacle and no-obstacle cases. Reynolds, Froude, and Richardson numbers are also comparable to previous studies; however, there was no clear relationship with the entrainment parameter. This suggests that entrainment dependency on non-dimensional parameters is not quantifiable where the analysis area length to lock-box length ratio is ≈ 1 . The presence of the obstacle was shown to increase entrainment by approximately 99% immediately downstream of the obstacle, associated with a subsequent entrainment decrease by 14% at the downstream end of the analysis area. For rectangular obstacles 1/6th the initial current height, as used for this study, an obstacle's role is limited in decreasing net velocity and entrainment and not fit-for-purpose as a barrier to reduce current velocity. Finally, we discuss optimization strategies, weighing up observed minimal net velocity/entrainment decrease with the detrimental effects of jet expansion. *Published by AIP Publishing.* [<http://dx.doi.org/10.1063/1.4979067>]

I. INTRODUCTION

Turbidity currents are a sediment-laden gravity flow, driven by buoyancy forces acting upon the density excess of a sediment-entrained fluid and an ambient, interstitial fluid, sharing a shear boundary. Such currents are commonly found in marine, limnic, and fluvial environments; however, the theory behind their driving mechanism holds the same for atmospheric events such as pyroclastic flows and haboobs. In some cases, such as sediment-laden freshwater river plumes, salinity and temperature can also contribute to the density imbalance. Turbidity currents are a known hazard to an ever-increasing number of marine installations. Pope, Talling, and Carter¹ provide a detailed review of recent subsea fiber-optic cable breaks from 1989 to 2015, of which a number were caused by turbidity currents. Turbidity currents also pose an increasing threat to offshore oil and gas pipelines, due to the rapid development of deep and ultra-deep oil and gas operations.² Consequently, the interaction of turbidity currents and saline-driven buoyancy currents (hereon referred to as “gravity currents”) with

obstacles has been the subject of a growing number of laboratory studies.^{3–9}

Sediment-laden underflows can be initiated by a range of natural geophysical sources, of which Meiburg and Kneller¹⁰ provide an extensive overview. They can also be initiated from a range of anthropologic activities such as dredging and bottom-trawling operations, which can re-suspend sediment and initiate current propagation.¹¹ Their propagation is typically divided into three phases of movement, defined by the dominant forces acting upon the current.^{12,13} During the initial slumping phase (the phase associated with the presented study), driving buoyancy forces dominate resistive inertial and viscous forces, causing the current head to propagate at a constant velocity. During the second, self-similar phase, current front velocity begins to decrease at an accepted rate of $\approx t^{1/3}$. During the third phase, resistive viscous forces dominate buoyancy and inertial forces, which causes a more rapid deceleration.¹³

The physical components of a turbidity current generally consist of a distinctive head, followed by a body and sometimes a tail.¹⁴ The head advances by displacing the ambient fluid, which is generally at rest.¹⁵ This displacement causes flow resistance of a greater magnitude than that caused by the bed friction or upper boundary layer of the current, rendering the head denser than the trailing body and tail. Bed

^{a)} Author to whom correspondence should be addressed. Electronic mail: rwil281@aucklanduni.ac.nz

^{b)} Email: h.friedrich@auckland.ac.nz

^{c)} Email: craig.stevens@niwa.co.nz

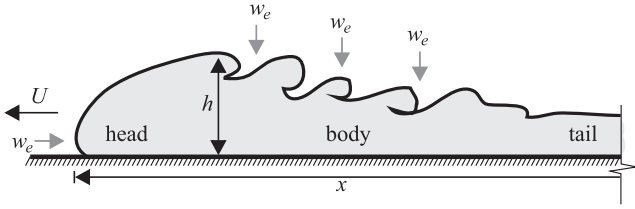


FIG. 1. Key anatomical components of a typical sediment-laden gravity flow through an interstitial fluid. Fluid is entrained into the current via overlapping at the current front and Kelvin-Helmholtz instabilities at the back of the head.

friction causes an overhanging nose to be formed that glides over the ambient fluid, entraining it into the current head (Figure 1). This results in a gravitational instability, producing three-dimensional lobate structures.¹⁵ Entrainment of the ambient fluid also occurs at the rear of the head. Shear stress at the upper boundary of the turbidity current and ambient fluid causes the formation of local instabilities, referred to as Kelvin-Helmholtz billows. These instabilities encourage mixing across the boundary, hence entrainment of the ambient fluid into the body of the turbidity current.

A. Dimensionless entrainment parameterization

In order to reliably predict the dynamic evolution of turbidity currents, it is vital to thoroughly understand entrainment.¹⁶ Morton, Taylor, and Turner¹⁷ were the first to postulate an entrainment law for gravity-driven plumes (hereafter referred to as the MTT hypothesis). They hypothesized that the rate of ambient entrainment into a current at a given location is proportional to a characteristic velocity of the current at that location,

$$E = \frac{w_e}{U}, \quad (1)$$

where E is the entrainment constant, w_e is the rate of entrainment, and U is a characteristic velocity of the current. Ellison and Turner¹⁸ used these principles to develop a theory which accounts for the stabilizing effect that occurs from the density difference across the boundary of the two fluids. They suggested that E is not constant, but rather a function, $E(Ri)$, of the overall Richardson number of the propagating current. Adopting this theory, Turner¹⁹ defined Ri as

$$Ri = \frac{g' \cos \theta}{U^2}, \quad (2)$$

where g' is the specific gravity, defined as

$$g' = g(\rho_0 - \rho_a)/\rho_a, \quad (3)$$

where ρ_0 is the initial density of the current, ρ_a is the density of the ambient water, and θ is the bed slope. Turner¹⁹ subsequently provided perhaps the most widely known empirical function of E , based on test results from Ellison and Turner,¹⁸

$$E = \frac{0.08 - 0.1Ri}{1 + 5Ri}. \quad (4)$$

Although (4) only holds valid for $Ri < 0.8$, Ellison and Turner¹⁸ showed that for larger Ri values, E becomes negligible due to the reduced mixing between fluid layers. Others have provided alternative empirical definitions of E for a

range of flow applications, as reviewed by Fernando.²⁰ More recently, Fernandez and Imberger²¹ reviewed key entrainment laws specific to buoyancy-driven underflows. Studies have also suggested that E is also a function of other flow parameters. Through laboratory experiments, Cenedese and Adduce²² investigated gravity currents propagating down a slope in a rotating fluid. Dense, saline fluid was released into ambient freshwater continuously at a constant rate. They showed that E was also dependent on the Reynolds number, defined as

$$Re = \frac{Uh}{\nu}, \quad (5)$$

where h is the current height, and ν is the kinematic viscosity of water. Alternatively, through field studies Fernandez and Imberger²¹ showed that E is a function of both Ri and bottom drag coefficient, C_D .

Previous studies have also investigated entrainment as a function of a densimetric Froude number. Fr is commonly expressed as

$$Fr = \frac{U}{\sqrt{g' h \cos(\theta)}}, \quad (6)$$

where θ is the bed slope angle. Based on the extensive research of previous studies, Sequeiros²³ showed that Fr values for both field and experimental buoyancy-driven currents tend to range between $Fr = 0-2$, centered on unity. Hence both subcritical and supercritical flow regimes are known to exist for turbidity currents in laboratory and field applications.

To the authors' knowledge, there are no experimental studies which explore how ambient entrainment in turbidity currents is affected by the presence of stand-alone obstacles. There is also a need to explore the relationship between E , Fr , Ri , and Re . Such studies are desired to provide insights into how the flow properties of turbidity currents are affected by submarine structures. In the present work, we experimentally investigate the effect a rectangular obstacle has on the mixing processes across the boundary layer of a turbidity current and ambient fluid. In particular, we aim to address the following three research questions:

1. What are the key stages of ambient fluid entrainment of turbidity currents upon interaction with a rectangular obstacle?
2. What effect does the obstacle have on net ambient entrainment into the current?
3. How are non-dimensional parameters affected by the presence of the obstacle?

Lock-exchange turbidity currents are released in a laboratory flume and their interaction with a single rectangular obstacle was captured using photometric techniques and density sampling. Key stages of entrainment are visually hypothesized and, based on the MTT entrainment hypothesis, we investigate their relationship with quantitative entrainment rates and non-dimensional parameters.

B. Area-augmented entrainment theory

In order to calculate E , U and w_e must be quantified. It is possible to measure U using photometric techniques that track the spatio-temporal movement of the current.^{16,24-26} However, there are no existing techniques suitable for directly measuring

w_e . Hence previous studies have indirectly defined w_e using theoretical relationships based on the conservation of mass and momentum. For a two-dimensional current flow over a planar surface, Turner¹⁹ showed that w_e can be expressed as

$$w_e = \frac{d(Uh)}{dx} = EU, \quad (7)$$

where h is the depth of the current, defined by integrals of the flow in the normal direction, z ,

$$Uh = \int_0^{\infty} u dz, \quad (8)$$

where u is the mean velocity relative to the velocity of the ambient fluid. More recent studies have provided alternative definitions for w_e . Through assuming E is independent of spatial position and using the MTT hypothesis, Cenedese, Whitehead, Ascarelli, and Ohiwa²⁷ showed that mean entrainment velocity can be defined as the ratio of the entrainment flow rate, Q_e , and planar basal area covered by the current, A_p ,

$$w_{em} = \frac{Q_e}{A_p} = \frac{1}{A_p} Q \left(\frac{1}{r_b} - 1 \right), \quad (9)$$

where Q is the input flow rate of dense fluid and r_b is a ratio of reduced gravity measured at varying distances from the input source and the reduced gravity of the current at the source. However, Cenedese and Adduce²² emphasized that when (9) is used in the MTT hypothesis (1), E is only valid for currents where the flow regime is constant. Therefore (9) is not suitable for studies incorporating obstacles, as U and w_e vary upon impact with the obstacle (as shown later). Additionally, conservation of mass cannot be preserved using only the planar area, as the current height varies considerably upon impact. Jacobson and Testik¹⁶ provided an alternative definition for w_e , which considers the two-dimensional side area of the current, A . They studied sediment-laden currents released by lock-exchange. They defined spatially averaged entrainment velocity as

$$w_e = \frac{U}{x} \frac{dA}{dx}, \quad (10)$$

where A was calculated through a photometric thresholding technique. In contrast to (9), (10) is appealing for studies incorporating obstacles as tracking the side-area of the current allows for variability in current height/length upon impact with the obstacle to be captured. Although (10) assumes that the flow is two-dimensional, cross-flume variability of the current boundary was seen to be considerably less significant relative to the variance in current height. The

additional spatial dimension of A in (10), as opposed to h in (9), can be seen as an improvement in quantifying the conservation of mass. However, photometric measurement techniques that could accurately track the spatial expansion of turbidity currents were not available at the time of Turner.¹⁹ Therefore (10) was adopted for this study.

II. EXPERIMENTAL SETUP AND METHODOLOGY

Lock-exchange experiments were carried out in an acrylic flume in the Hydraulic Engineering Laboratory at the University of Auckland. The flume had a 5 m base length (x_L), 400 mm base width, and was set at a slope of $\theta = 2\%$. The lock-box at the upstream end had a width of 580 mm and a 400 mm wide manual release gate. Likewise, the sump at the flume bed terminus had a length of 580 mm and a depth of 660 mm. The function of the sump was to dampen wave reflections of the generated current off the end wall. A 50 mm high, 140 mm wide rectangular obstacle of interest which spanned the width of the flume was located at $x = 3700$ mm from the lock-box gate. The acrylic obstacle was installed at this location to allow surface disturbances time to dissipate prior to the arrival of the current. A rough substrate, consisting of $D_{50} = 0.85$ mm sand glued to a 4000 mm steel sheet, was installed on the flume bed for various experimental runs. It was of interest to investigate its role in ambient entrainment over the obstacle as past studies have shown E to increase over rough substrates.²⁴

Two arrays of 10 siphon tubes were located before and after the obstacle to collect 25 ml density samples of the passing currents (Figure 2). These arrays were located 100 mm from the side wall of the flume. The siphons were controlled automatically by pneumatic valves connected to a vacuum, which were triggered when the head of the current passed the respective array. Before the release of currents, all the siphon tubes were purged, ensuring no ambient fluid was entrapped. Fluid density was subsequently measured from the samples using 20 ml and 25 ml volumetric flasks.

The passage of currents through a designated analysis area, centered around the obstacle, was captured using a Lumenera LT425 CMOS 4.0-megapixel camera with a NIKKOR 50 mm $f/1.8$ fixed lens. The analysis area had a height of 350 mm and width 590 mm. For each run, the 2048-pixel width of the camera frame was aligned with the horizontal extents of the analysis area, which was outlined with a ruler attached to the flume wall. The 1504-pixel height of the frame was aligned with a similar vertical ruler.

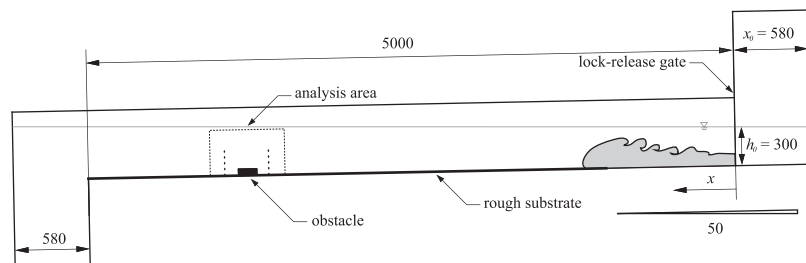


FIG. 2. Schematic diagram of experimental acrylic flume. A lock box and release gate were located at the upstream extent, where h_0 is the initial ambient fluid height and x is the bed distance measured from the gate location. The rectangular obstacle was located at $x_f = x/x_0 = 6.38$, and the photometric analysis area is outlined with a dashed line. The upstream density profiles, ρ_u , were measured at $x_f = 6.21$ and downstream density profiles, ρ_d , were measured at $x_f = 6.79$. Density measurement locations are shown as points within the analysis area.

TABLE I. Experimental parameters of completed flume tests.

Experiment number	Substrate/obstacle condition	T (°C)	ρ_0 (kg m ⁻³)	ρ_a (kg m ⁻³)	g' (ms ⁻²)	Volumetric concentration, S_0 (%)	Kinematic viscosity, ν (m ² s ⁻¹)	Re_{IQR} (-)	Ri_{IQR} (-)	Fr_{IQR} (-)
A1	Smooth bed/no obstacle	22.5	1020	997.66	0.22	0.57	9.94×10^{-7}	15 400-23 600	4.01-5.57	0.42-0.50
A2	Smooth bed/no obstacle	18.5	1040	998.5	0.41	1.08	9.87×10^{-7}	26 200-39 300	2.86-3.50	0.53-0.59
A3	Smooth bed/no obstacle	18.5	1060	998.5	0.6	1.57	9.80×10^{-7}	32 100-43 400	3.41-4.05	0.50-0.54
A4	Smooth bed/no obstacle	18.5	1080	998.5	0.8	2.08	9.74×10^{-7}	46 600-54 900	2.41-3.82	0.51-0.64
B1	Rough bed/no obstacle	22	1020	997.77	0.22	0.57	9.94×10^{-7}	17 500-22 600	4.40-6.99	0.38-0.48
B2	Rough bed/no obstacle	23	1040	997.54	0.42	1.08	9.88×10^{-7}	25 500-37 200	2.96-4.26	0.48-0.58
B3	Rough bed/no obstacle	21.5	1060	997.88	0.61	1.59	9.81×10^{-7}	31 100-45 200	2.96-3.72	0.52-0.58
B4	Rough bed/no obstacle	22	1080	997.77	0.81	2.10	9.75×10^{-7}	44 400-54 600	3.12-4.51	0.47-0.57
OA1	Smooth bed/obstacle	19	1020	998.41	0.21	0.55	9.94×10^{-7}	11 500-17 500	9.09-21.75	0.21-0.33
OA2	Smooth bed/obstacle	20	1040 ^a	998.2	0.42	1.10	9.87×10^{-7}	21 700-30 400	4.02-12.98	0.28-0.50
OA3	Smooth bed/obstacle	19	1060	998.41	0.61	1.57	9.81×10^{-7}	25 400-34 000	5.48-12.84	0.28-0.43
OA4	Smooth bed/obstacle	18	1080	998.6	0.8	2.08	9.74×10^{-7}	29 400-42 100	3.66-19.01	0.23-0.52
OB1	Rough bed/obstacle	21	1020	997.99	0.22	0.56	9.94×10^{-7}	13 500-17 900	5.69-17.49	0.24-0.42
OB2	Rough bed/obstacle	23	1040	997.54	0.42	1.08	9.88×10^{-7}	22 200-27 600	4.47-11.67	0.29-0.47
OB3	Rough bed/obstacle	21.5	1060	997.88	0.61	1.59	9.81×10^{-7}	30 000-36 800	4.44-10.15	0.31-0.47
OB4	Rough bed/obstacle	21.5	1080	997.88	0.81	2.10	9.74×10^{-7}	28 200-34 200	6.62-16.40	0.25-0.39

^aInitial theoretical density was 1040.89 kg m⁻³ due to a measurement error, however it is referred to as 1040 kg m⁻³ for simplification.

Illumination of the flume comprised eight 500 W halogen lamps located parallel to the flume wall and above the obstacle. Further details regarding camera placement and illumination are given in the work of Wilson.²⁸

A total of 16 experimental runs were conducted with four different substrate/obstacle and initial density configurations. The sediment mixture used to create the varying initial current densities was comprised of a 1:1 ratio by mass of kaolinite clay and spherical glass beads (Table I). Initial tests showed that the head difference between the lock-box and ambient water, caused by the addition of the sediment slurry to the lock-box, created significant surface waves upon the release of the gate. Therefore, the equivalent slurry volume was displaced from the lock-box.

For all experimental runs, the flume was first filled with tap water to a height of $h_0 = 300$ mm at the lock-box gate. Next, the sediment slurry was mixed for a minimum of 30 s and ambient water temperature was noted. The halogen lights were then turned on, to minimize the creation of temperature gradients, hence convective currents within the ambient fluid. Next, a Canon 60D reference camera was triggered and the volume of displacement fluid in the lock-box was removed. The slurry was mixed for an additional 10 s prior to being added to the lock-box. Thereafter the gate was released, causing a turbidity current to form. The LT425 camera began recording at $x/x_0 \approx 4.3$ m and ceased at a minimum of 30 s after the current had passed the obstacle.

The raw images were recorded at a framerate of 120 Hz, resulting in one of the fastest-sampled visual datasets of experimental turbidity currents. A high framerate was desired to adequately capture detail of the current as it interacts with the obstacle.

To post-process the images, a binary image thresholding technique was applied through a series of processes to delineate the current boundary. First, barrel lens distortion was removed from the images through batch processing in

Adobe Photoshop CS6. The images were then spatially calibrated in MATLAB by converting the mean of three pixel measurements of the known distance between instrument racks within the analysis area to metric values. The resulting resolution ranged from 0.307 to 0.310 mm pixel⁻¹. Measurements were taken between the upstream and downstream instrument racks as they were located along the centerline of the flume. This allows the most practical representation of the current front position when taking into account the change in camera perspective. We validated it by calculating spatial calibration factors at the front and back walls of the flume, which showed that the adopted factors had an error of -4.4% and +6.0% when calculating current nose velocity, U .

To improve contrast, the mean background of images captured prior to current arrival was subtracted from each analyzed image. Images were then rotated, converted to greyscale, and cropped. Next, the image was reduced to a binary resolution by identifying the pixel intensity value that came closest to matching the visible turbidity-ambient interface. The detected boundary was then delineated, allowing the spatial dimensions of the current to be quantified, such as the current nose location, x , and U . Current height, h , was taken as the highest point of the current boundary within the analysis area. Total current area, A , was calculated as the area of the delineated current within the analysis area, A_{obs} , plus the approximated current area between the lock-box gate and the analysis area, A_{lock} . Nogueira, Adduce, Alves, and Franca²⁴ showed that the bulk current height is $\approx 1/3h_0$. Therefore, A_{lock} was approximated as $1/3h_0$ multiplied by the known length of the lock-box to the analysis area ($x/x_0 = 6$). It could be argued that this assumption may not be suitable for sediment-laden currents, given Nogueira *et al.* conducted studies using saline currents over a flat bed. However, for the present study we are concerned with dA/dx , thus it will have no effect on entrainment parameterization.

III. RESULTS AND DISCUSSION

A. Basic flow qualities

Upon the release of the lock-box gate, gravity acted upon the density difference of the two fluids causing the sediment-laden fluid to collapse. Buoyancy forces caused the current to propagate forwards, and bed friction caused a typical overhanging nose to form at the head of the current. This was evident for all tests. For tests without the obstacle, horizontal front velocities of the current were found to be relatively consistent, with minor local fluctuations, when travelling through the analysis area. This confirms that all currents were within the phase upon arrival at the analysis area, in line with Rottman and Simpson,¹³ who have shown that the location of the transition between slumping and self-similar phases occurs at a distance of approximately 5–10 times the lock-box length.

A key objective of this paper is to investigate how the presence of a basal obstruction affects the entrainment of the ambient fluid into the sediment-laden current. Therefore, significant visual flow characteristics and their potential effect on fluid entrainment were identified. For the eight tests with obstacles, four different flow stages were observed as the current interacted with the obstacle:

- (i) *Lateral entrainment stage.* Upon impact with the obstacle, the nose rapidly decelerated and was deflected both upwards and laterally along the face of the obstacle (Figure 3(a)). The lateral deflection of the frontal instabilities, combined with the continued forward movement of the current, appeared to trap the ambient fluid in a column-like feature. The combined forwards and upwards movement caused the current to shear off the top edge of the current, creating an irrotational vortex.
- (ii) *Jet stage.* The upwards deflection of the current acted as a jet, causing the current to detach from the bed and expand vertically (Figure 3(b)). A similar characteristic was also observed in previous studies.^{3,29,30} A large Kelvin-Helmholtz instability forms at the upstream

extent of the jet expansion. The jet appears to facilitate the growth of the frontal vortex, which visibly entrains the ambient fluid at the nose and recirculates it into the head. As expected, the size of the vortex and jet increased for tests with higher densities.

- (iii) *Collapsing stage.* The height of the jet expansion eventually plateaued when gravitational forces exceeded force scales with the rate of change in momentum (Figure 3(c)). Simultaneously, the front of the current sheared off the downstream edge of the obstacle, creating a secondary irrotational vortex that visibly entrained the ambient fluid. The sudden downwards expansion of the current, coupled with the forward deceleration, caused a blunt, rectangular front to form. This front subsequently collapsed concurrently with the jet, emulating a similar process as the initial removal of the lock-box gate. The current is partially reflected off the obstacle back towards the lock-box, causing a typical hydraulic jump to form.^{3,30,31} The hydraulic jump appeared to assume the form of an undular bore, rather than a sharp, turbulent bore.
- (iv) *Re-establishment stage.* Upon reattachment with the flume bed, the current head began to re-establish downstream, leaving a noticeable gap at the rear of the head where a large Kelvin-Helmholtz instability forms (Figure 3(d)). This suggests that the flow over the obstacle edge enters a supercritical state, eventually transitioning to a quasi-steady, subcritical state. This is consistent with previous studies.^{3,7,30–32}

B. Temporal entrainment parameterization

Figure 4 shows the fractional current area, $A_f = A/A_0$, as a function of $x_f = x/x_0$, where A_0 is the cross-sectional area of the lock-box. It can be seen that for tests without the obstacle, $A_f(x_f)$ develops a linear function, confirming that the current is still within the slumping phase at the location of the obstacle. This is in line with previous studies which show that the dimensionless area increases linearly with the dimensionless

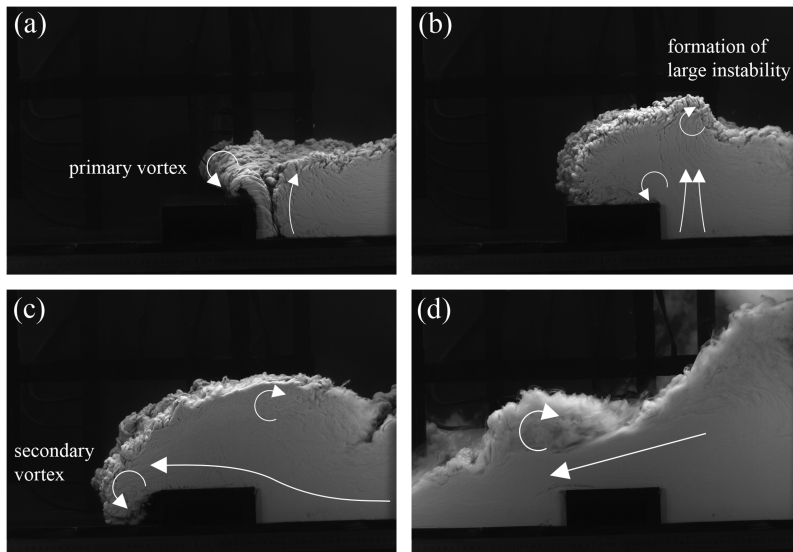


FIG. 3. Identified flow stages of the observed current traversing the rectangular obstacle: (a) lateral-entrainment stage, (b) jet stage, (c) collapsing stage, and (d) re-establishment stage.

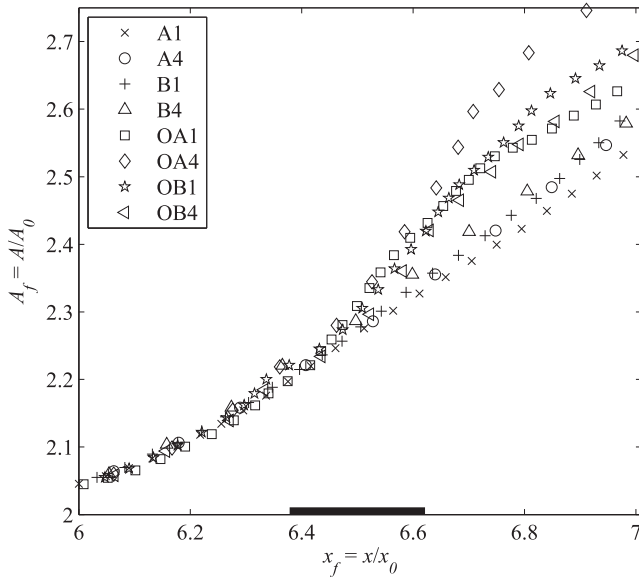


FIG. 4. Dimensionless current area as a function of dimensionless distance. The horizontal extent of the obstacle is shown in black. For tests without the obstacle, an approximate linear relationship develops above $x_f = 6.3$. Tests with the obstacle show a clear increase in the dimensionless area from $x_f = 6.5$. For clarity, some tests have been omitted and only every 32nd data point is plotted.

current distance during the slumping and inertia-buoyancy phases.^{16,33} However, all obstacle runs show a noticeable increase in A_f flux (dA_f/dx_f) between $x_f = 6.4$ - 6.7 , showing the obstacle causes a rapid expansion of A_f . By the conservation of mass, this corresponds to an increase in the entrainment rate of the ambient fluid. Interestingly, the shape of $A_f(x_f)$ in Figure 4 is similar to that of an unobstructed current transitioning from the inertia-buoyancy phase to the viscous-buoyancy phase.¹⁶ This is understandable, as it has been shown that during this transition, the current rapidly decelerates, followed by a sudden increase in the height.¹⁶ For both obstacle configurations, dA_f/dx_f increases with increasing initial volumetric concentration, S_0 .

The downstream density profiles (measured at $x_f = 6.79$ as shown in Figure 2) for runs A1-4 show a decrease in density with increasing height (Figure 5(a)). The stratifications appear to resemble a typical smooth profile shape, similar to the results of Jacobson and Testik³⁴ for currents of $S_0 = 5.4\%$ measured at a distance of $x_f = 1.35$ - 1.53 . Tests B1-4 (not presented) also showed similar profiles, although the measurements tended to show a greater amount of dilution from S_0 . This can be attributed to bed friction causing a greater reduction in near-bed velocity, resulting in a greater settlement of the suspended sediment or a higher detrainment of the sediment relative to the entrainment of the ambient fluid.

Downstream density profiles for obstacle runs with a higher S_0 show a typical plume-like profile, whilst runs OA1-2 show a smoother profile (Figure 5(b)). Interestingly, Jacobson and Testik³⁴ showed that a plume-like profile precedes a smooth profile for currents of similar concentration. This agrees with our observations of the current re-establishment after the obstacle, with similar visual characteristics to the initial propagation at the lock-box. This observation was more visible for currents with higher densities. The presence of the obstacle also causes a greater reduction in downstream densities, relative to runs without the obstacle. This is shown in Figure 6(a), where the currents are seen to have a global density decrease of up to $(\rho_u - \rho_d)/\rho_0 \approx 0.03$ over the obstacle for runs OA2-4. Yet runs without the obstacle showed a general decrease in density of only up to $(\rho_u - \rho_d)/\rho_0 \approx 0.02$ (Figure 6(c)).

Intriguingly, runs OB1-4 showed higher density differences than runs OA1-4 (up to $(\rho_u - \rho_d)/\rho_0 \approx 0.04 \text{ kg m}^{-3}$), whilst runs B1-4 show no obvious difference to runs A1-4 (Figures 6(a)-6(d)). This suggests that the combination of the obstacle and substrate amplifies the net drag effect experienced by the current. As expected, Figure 6 shows for each obstacle configuration the density difference tends to increase with increasing S_0 . Most runs show a density decrease between upstream ($x_f = 6.21$) and downstream measurements, which adds to the conflicting arguments of previous studies

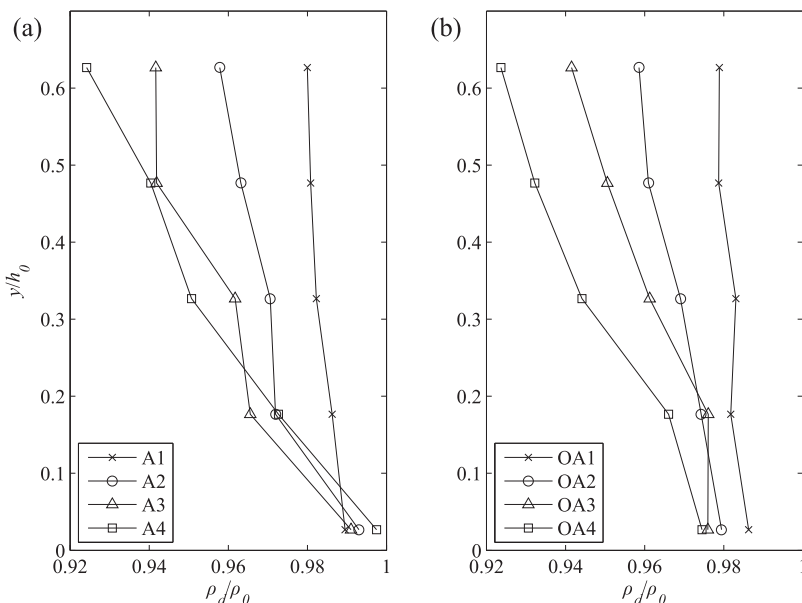


FIG. 5. Measured raw downstream non-dimensional density profiles of the test currents. (a) Runs A1-4 which exemplify the typical stratification profiles downstream of the obstacle, and (b) runs OA1-4, exemplifying the typical stratification profiles of runs without the obstacle.

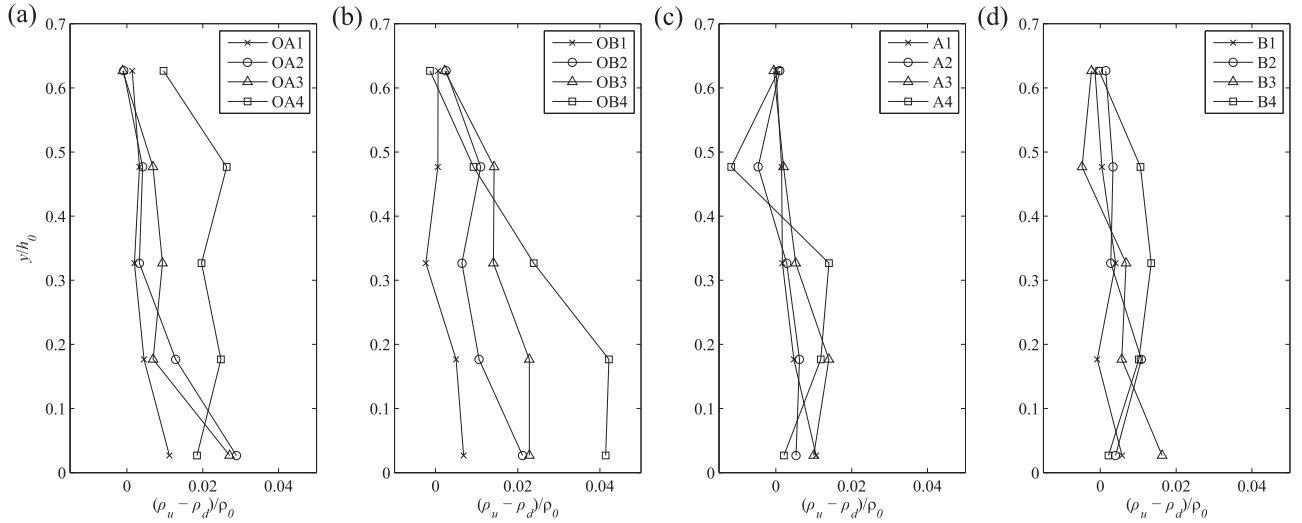


FIG. 6. Measured raw non-dimensional difference of upstream and downstream density profiles. Non-dimensional height is plotted as a function of $(\rho_u - \rho_d)/\rho_0$, where ρ_u is measured density from the upstream siphon and ρ_d the measured density of the corresponding downstream siphon. (a) Runs with obstacle over a smooth substrate, (b) runs with obstacle over a rough substrate, (c) no-obstacle runs over a smooth substrate, and (d) no-obstacle runs over a rough substrate.

identified by Jacobson and Testik.³⁴ Some studies argue that during the slumping phase, no dilution occurs within the current head,^{35,36} whilst others have shown that some dilution occurs.^{24,33,34} The results of this study thus bolster the agreement that in fact dilution does occur in the head during the slumping phase, albeit minimal.

To evaluate (1), w_e was calculated using (9). As expected, the non-dimensional form of dA , dA/A_0 , showed a rapid increase as the current entered the analysis area due to the imposed virtual extents of current delineation (Figure 7). A similar increase would be expected when the lock-box gate is opened. However, when the current reaches the analysis area, dA/dx is likely to remain constant for the runs with no obstacle, as U and h were seen to be relatively consistent at this location from the reference videos. Jacobson and Testik¹⁶ also showed dA/dx to be consistent for sediment-laden currents. Figure 7(a) shows the rapid increase in dA to occur prior to the arbitrary distance of $x_f \approx 6.29$. Therefore, dA values within this range were replaced with the mean of all values of $x_f > 6.55$, for each respective run. Likewise, dA for all runs with obstacles was adjusted where $x_f \lesssim 6.29$; however, it was replaced with the mean of $x_f > 6.55$ for the corresponding run with no

obstacle as it was assumed that prior to interaction with the obstacle, the respective currents would hold similar values in dA (Figure 7(b)).

No-obstacle runs show w_e to be relatively consistent over non-dimensional distance, x_f (Figure 8(a)). This agrees with visual observations described in Sec. III A, where no significant change in current height or U was observed. There is a clear relationship between S_0 and w_e , where w_e is shown to be greater for higher S_0 . This can be attributed to the positive relationship between S_0 and U . However, there is no distinctive difference between smooth substrate runs and their rough counterparts. Run A4 shows on average the highest entrainment velocity, $w_e \approx 1.2 \text{ cm s}^{-1}$, whilst all other runs vary between $w_e \approx 0.4 \text{ cm s}^{-1}$ and $w_e \lesssim 1.2 \text{ cm s}^{-1}$. Jacobson and Testik¹⁶ showed that temporal entrainment velocity decreases with distance from the lock-box and eventually tends towards zero upon entering the viscous-buoyancy stage. This cannot be confirmed for this study, given our focus on the small spatial measurement window relative to the flume length ($x_A/x_0 \approx 1.03$); however, where the obstacle is absent, w_e is expected to also tend towards zero, as dA/dx and U appeared to remain consistent in the reference videos. The range of w_e in this study

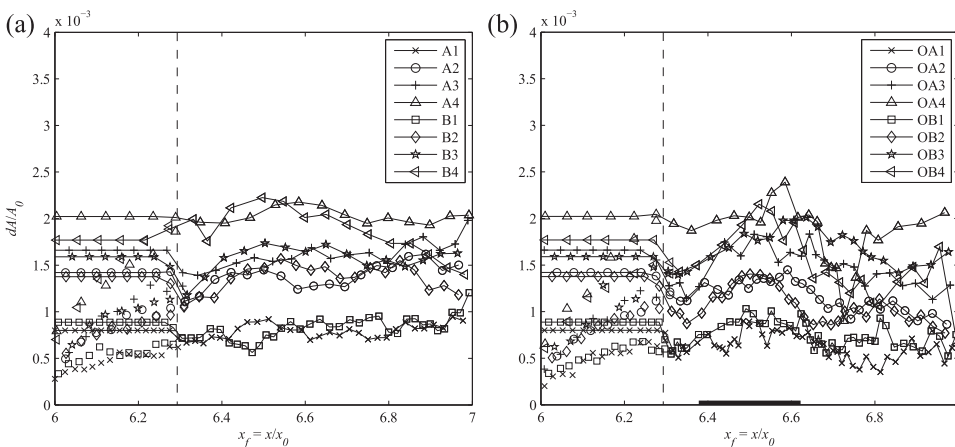


FIG. 7. dA/A_0 as a function of x . For clarity, data has been smoothed time-wise and only every 16th data point is plotted. dA values prior to $x_f = 6.29$ have been replaced with the average of dA for $x_f > 6.55$. Non-manipulated values are shown as standalone data points. (a) No-obstacle runs and (b) obstacle runs.

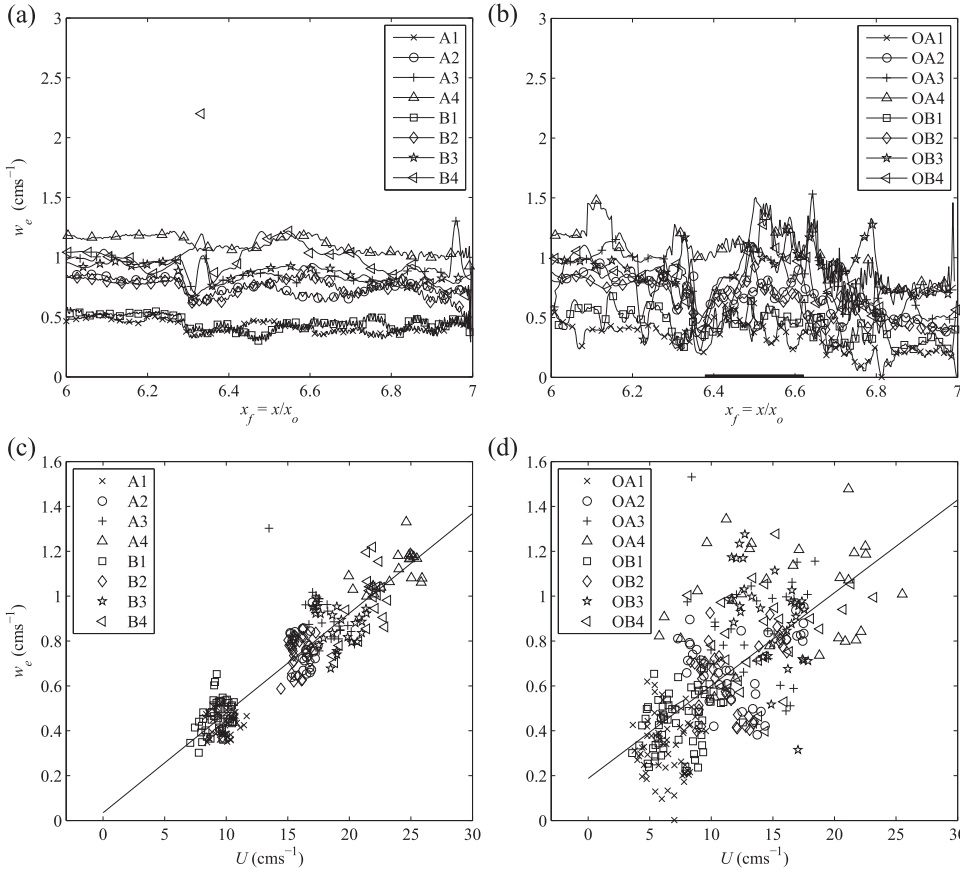


FIG. 8. Temporal entrainment velocity, w_e , as a function of non-dimensional distance from the lock-box, x_f , and nose velocity, U . For clarity, only every 16th value over time is plotted. (a) $w_e(x_f)$ for no-obstacle runs, (b) $w_e(x_f)$ for obstacle runs, where the horizontal extent of the obstacle is shown in black. (c) $w_e(U)$ for no-obstacle runs fitted with a linear function, and (d) $w_e(U)$ for obstacle runs fitted with a linear function.

is comparable to Jacobson and Testik,¹⁶ who also showed w_e to be less than unity where $x > 3.48$ m. Figure 8(b) shows a contrast to the no-obstacle runs, where the currents have distinctive characteristics that can be paired with the current stages outlined in Sec. III A. In the region before the obstacle, all runs show a general decrease in w_e ($x_f = 6.3$ - 6.4), however a small local spike is evident for runs OA1, OA2, OB1-4. The spike caused a sudden decrease in dx as the nose rises up the face of the obstacle. This is followed by a steady increase in w_e over the top of the obstacle. This increase is due to an increase in dA/dx caused by the jet expansion after impact with the obstacle. w_e is then shown to plateau at $x_f = 6.5$ - 6.6 and subsequently to decrease to a point after the obstacle where it stabilises. This agrees well with visual characteristics of the jet reaching a plateau and consequently collapsing, followed by a re-establishment stage.

Next, w_e was investigated as a function of U . Jacobson and Testik¹⁶ showed that temporal entrainment velocity is not influenced by U during the initial stages of the slumping phase. Their results showed w_e to initially decrease independently of U . However, they showed that a highly dependent relationship was formed at lower values of U upon the transition into the inertia-buoyancy phase, where w_e decreased proportionately to U . Therefore, it was of interest to see if such a relationship occurred in the present study, and how any relationship may be affected by the presence of the obstacle. All eight no-obstacle runs showed w_e to hold a scattered relationship with U , giving no clear evidence that w_e initially increased independently to U (Figure 8(c)). This is understandable as capturing the initial rapid increase in dA/dx at the lock-box gate was outside

the scope of this study, which has previously shown the initial independence of w_e to U .¹⁶ In contrast to each individual run, linear regression shows that there is a strong global trend evident, where w_e increases with U (R-squared = 0.85). This is due to runs with higher S_0 showing on average a greater w_e and U than those with lower S_0 . The MTT hypothesis therefore holds true for runs with no obstacles, with the linear equation represented as

$$w_e = a_1 U + b_1, \quad (11)$$

where empirical coefficients $a_1 = 0.044 \text{ m s}^{-1}$ and $b_1 = 0.035 \text{ m s}^{-1}$. Although weaker, Figure 8(d) shows there is also a global trend where w_e increases with increasing U , with variance in w_e increasing at higher values of U . An increase in scatter was also observed by Jacobson and Testik,¹⁶ who postulated that it was due to adjustments associated with the current transitioning from the slumping phase to the inertia-buoyancy phase. As it has been shown, with the analysis area of this study being within the distal limits of the slumping phase, the increasing scatter adds to the theory (as illustrated in Figure 4(b)) that the presence of the obstacle causes the current to either experience similar characteristics to the inertia-buoyancy phase or initiate the transition prematurely. The trend in Figure 8(d) can be represented by the following linear function:

$$w_e = a_2 U + b_2, \quad (12)$$

where $a_2 = 0.041 \text{ m s}^{-1}$ and $b_2 = 0.187 \text{ m s}^{-1}$ with an R-squared value of 0.42. Therefore the MTT hypothesis may hold true for the case of obstacles; however, the relationship is clearly much weaker than Figure 8(c).

To investigate how the obstacle affected the entrainment of the ambient fluid into the current, entrainment parameter, E , was plotted as a function of x_f (Figure 9). E was determined using (1). For runs with no obstacle, E is shown to have a minor variance, with a range of $E \approx 0.04$ - 0.06 , which is a reflection of the constant U and w_e of the currents (Figure 9(a)). E can be seen to be slightly higher for $x_f < 6.29$, which is a result of the manipulation of dA . In comparison to other studies, E is shown to overlap with the upper limits of experimental gravity currents studied by Cenedese and Adduce.²² Interestingly, E was higher than that measured by Jacobson and Testik,¹⁶ who conducted tests with generally denser currents ($\rho_0 \approx 1033$ - 1198 kg m^{-3}). Several factors may explain this discrepancy, for example, the present study had a sloped bed that contributes to the inertial driving forces of the current. The present study also incorporated spherical glass beads in the sediment mixture, which may have aided entrainment, given it visibly settled faster than kaolinite.

For runs with the obstacle, there is a characteristic change in E over x_f . Prior to the obstacle, all runs show a sharp peak

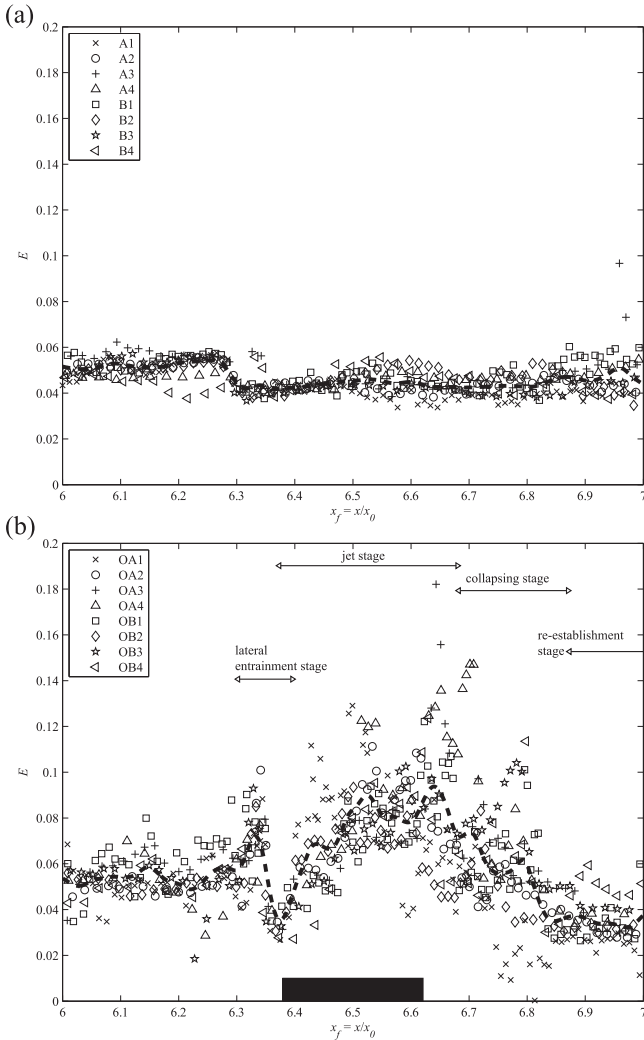


FIG. 9. Entrainment parameter, E , as a function of non-dimensional distance x_f . For clarity, every 8th value over time has been plotted. The horizontal extent of the obstacle is shown in black. (a) No-obstacle runs and (b) obstacle runs. A smoothing spline curve function was fitted to show the general changes in E for all runs.

in E ($x_f \approx 6.35$ - 6.36) (Figure 9(b)). This is a result of the increase in w_e (Figure 8(b)), coupled with the momentary decrease in front velocity, U , due to the nose rising laterally and vertically up the obstacle face. Therefore, this agrees well with the identified lateral entrainment stage in Sec. III A. There is a gradual increase of E over the obstacle for all runs, where OA3 shows E values up to approximately 0.19. Based on the lines of fit, E was found to be approximately 99% greater at the downstream obstacle edge ($x_f \approx 6.62$) than at no-obstacle tests. This is related to the rapid expansion of the jet ($x_f \approx 6.4$ - 6.65) within the jet expansion stage. E then shows a gradual decrease as the current shears off the back of the obstacle and forms the characteristic blunt nose, related to the collapsing stage ($x_f \approx 6.65$ - 6.9). Finally, E is shown to become somewhat consistent in the range of $E \approx 0.02$ - 0.06 , which is analogous to the re-establishment stage, where U and dA/dx stabilise. Interestingly, E is shown to be approximately 14% less than no-obstacle tests at $x_f = 7$, based on the lines of fit. The overall range in E for obstacle runs was much greater (≈ 0.01 - 0.18) than that for no-obstacle runs. This range overlaps with field investigations by Princevac, Fernando, and Whiteman³⁷ and also experimental gravity flows at various slopes by Ellison and Turner.¹⁸

Next, the influence of the obstacle on non-dimensional flow parameters was investigated. Interquartile ranges (IQRs) of temporal Richardson, Reynolds, and densimetric Froude numbers were calculated using (2), (5), and (6), respectively (Table I). Overall, Re ranged from 11 500 to 54 900, which is in line with previous studies. Adduce, Sciortino, and Proietti,³⁸ who studied saline currents, measured Re values between 2260 and 38 724 for similar densities of $\rho_0 = 1031$ - 1090 kg m^{-3} . As expected, Re increased with increasing S_0 . The rough substrate is shown to have a negligible effect on Re for both obstacle and no-obstacle conditions, reinforcing its limited role in ambient entrainment. The presence of the obstacle, however, caused on average a 20% decrease in mean Re for smooth tests. This can be attributed to the reduction in U .

For all tests, the overall IQR of Fr is situated in the subcritical flow regime (0.21-0.64). This range is seen to overlap with other studies, however in general Fr is much lower relative to the higher values of E . Similar to Re , mean Fr is reduced by 33% for obstacle tests on a smooth substrate, relative to their no-obstacle counterparts. This is explained by the jet expansion causing a higher height-to-nose-velocity ratio, hence a smaller Fr . The IQR is also greater for obstacle tests, which can be attributed to varying U and h throughout the analysis area.

Finally, Richardson number, Ri , was determined, where $\theta = \tan^{-1}(2/100)$. The runs showed Ri to decrease with increasing S_0 , which is to be expected as higher densities render higher U and boundary turbulence, hence more mixing and less stratification. Jacobson and Testik¹⁶ found that Ri had a range of approximately 3-13 for kaolinite-based currents of $\rho_0 = 1058 \text{ kg m}^{-3}$. This agreed well with obstacle tests OA3 and OB3 ($\rho_0 = 1060 \text{ kg m}^{-3}$) which showed a range of 4.44-12.84. Tests without the obstacles where $\rho_0 = 1060 \text{ kg m}^{-3}$ (A3 and B3) showed a lower range of 2.96-4.05. This difference is likely due to their relatively consistent U , whereas

obstacle tests showed reduction in U upon collision with the obstacle, resulting in larger Ri values.

C. Implications of obstacle effect on entrainment and mixing

The main objective of the present study was to investigate how the entrainment of the ambient fluid was affected by the presence of a rectangular obstacle. This was realised by examining whether key qualitative characteristics of the observed current-obstacle interaction correlate to measured entrainment parameters. The high framerate of the camera was found to provide significant details of flow characteristics surrounding the obstacle, supporting its use for future obstacle studies.

The presented results support the MTT hypothesis to a degree, where the entrainment velocity is correlated to a characteristic current velocity. Higher initial current densities were shown to produce higher entrainment velocities, although initial current density did not appear to explicitly influence E for no-obstacle runs as opposed to other studies.^{16,24,33} Upon re-establishment of the current head, however, E appeared greater for obstacle runs with higher S_0 . Substrate roughness at the measured scale was also found to play an insignificant role in influencing E and no distinctive difference in entrainment velocity between smooth and rough runs. Although upon reaching the end of the analysis area, the substrate runs were shown to have greater E than their obstacle counterparts. For some runs, Nogueira, Adduce, Alves, and Franca²⁴ found E to be greater for rough substrates; however, there was no distinctive trend in the present results.

A key outcome of this study was that the variation in the entrainment parameter over the obstacle agreed well with the four different characteristic stages identified in Sec. III A. At the downstream end of the obstacle, E was shown to be $\approx 99\%$ higher than that for the no-obstacle runs. This highlights the increased entrainment due to jet expansion and vortices formation. At the downstream end of the analysis area, the mean E for obstacle runs was shown to be $\approx 14\%$ less than that for no-obstacle runs. However, at the downstream extent, entrainment was shown to increase towards values seen for no-obstacle runs.

The obstacle was found to reduce both Fr and Re numbers, and increase Ri numbers, which tended to fit within the range of previous studies. There was no clear evidence that E held a relationship with Fr , Re , or Ri when considering the analysis area surrounding the obstacle ($x_A/x_0 \approx 1.03$). This suggests that a relationship between E and non-dimensional numbers may only be evident when tracking current propagation over the entire experimental flume and not comparatively small focal areas.

Bulk parameterisation was not considered, as the focus of this study was on the temporal and spatial development of entrainment over the obstacle. However, there is particular merit in future tests exploring bulk parameters that encompass the complete propagation of the current from the lock-box to the flume terminus. Such studies would help clarify the whole-of-life entrainment characteristics, particularly how entrainment develops after current reattachment. This is of interest, as the present results show that E reaches to a value

less than that of no-obstacle tests. However, it may return to a comparable value downstream. The practical implications of this suggests that a rectangular obstacle with a height-to-initial water height ratio of $0.05/h_0 \leq 1/6$ used as a protective barrier to stop the propagation of turbidity currents may have some effect in reducing re-established current velocity. However, when considering the effect an expanding jet would impose on water turbidity, and the subsequent detrimental repercussions for flora and fauna, the entrainment/velocity reduction may not outweigh environmental implications.

IV. CONCLUSIONS

Lock-exchange experiments investigating how the entrainment of the ambient fluid is affected by the presence of a rectangular obstacle were conducted. A total of 16 tests were completed, with varying initial density and bed roughness. The evolution of the entrainment parameter over the obstacle was discussed and paired with visual characteristics of significance. Subsequently, the relationship between entrainment and non-dimensional parameters was investigated and discussed.

The MTT hypothesis was shown to be true for no obstacle runs, where U maintained a positive relationship with w_e . For the case of obstacle runs, there was a weaker positive relationship between U and w_e of R-squared = 0.42. Therefore, further studies are needed over a greater spatial area to determine the validity of the weak relationship. Dilution was found to occur during the slumping phase, adding to the argument of conflicting studies. In addition, the incorporation of a rough basal substrate had no significant effect on density profiles or entrainment.

The key objective of our study was to determine new insights into the entrainment mechanics upon collision, hence an analysis area that focused on the immediate range of the obstacle was used. The entrainment parameter, E , for both obstacle and no-obstacle runs was comparable to previous studies. Four stages of entrainment over the obstacle were visually identified and later confirmed with quantitative results: (i) lateral entrainment stage; (ii) jet stage; (iii) collapsing stage; (iv) re-establishment stage. The presence of the obstacle caused E to increase by $\approx 99\%$ of no-obstacle runs at the downstream face due to the jet expansion and vortices formed by flow detachment. Upon re-establishment of the current after the obstacle, E was shown to be on average $\approx 14\%$ less than that for no-obstacle runs. However, there is potential for the current to resume to comparable E downstream of the analysis area, which is an aspect worth considering in future research. Although our study found Reynolds, Richardson, and Froude numbers comparable with other studies, there was no discernible relationship with E . This suggests that such a relationship cannot be determined without analyzing current propagation over the extent of the experimental flume. Our findings also suggest that although a rectangular obstacle of dimensions $0.05/h_0 \leq 1/6$ causes a local reduction in E , there is no significant residual decrease upon re-establishment of the current. In practical terms, obstacles of such dimensions used in the field to reduce current entrainment/velocity may also need to consider the detrimental effects of jet expansion on flora and fauna.

ACKNOWLEDGMENTS

We would like to thank Trevor Patrick, Geoff Kirby, and Jim Luo for their help in constructing and installing required experimental components. We would also like to thank the reviewers for their constructive comments which aided us in improving the quality of the manuscript.

- ¹E. L. Pope, P. J. Talling, and L. Carter, "Which earthquakes trigger damaging submarine mass movements: Insights from a global record of submarine cable breaks?," *Mar. Geol.* (in press).
- ²R. Bruschi, S. Bughi, M. Spinazzè, E. Torselletti, and L. Vitali, "Impact of debris flows and turbidity currents on seafloor structures," *Norw. J. Geol.* **86**, 317 (2006).
- ³E. Ermanyuk and N. Gavrilov, "Interaction of internal gravity current with an obstacle on the channel bottom," *J. Appl. Mech. Tech. Phys.* **46**, 489 (2005).
- ⁴C. Oehy and A. Schleiss, "Control of turbidity currents in reservoirs by solid and permeable obstacles," *J. Hydraul. Eng.* **133**, 637 (2007).
- ⁵O. E. Sequeiros, B. Spinewine, M. H. Garcia, R. T. Beaubouef, T. Sun, and G. Parker, "Experiments on wedge-shaped deep sea sedimentary deposits in minibasins and/or on channel levees emplaced by turbidity currents. Part I. Documentation of the flow," *J. Sediment. Res.* **79**, 593 (2009).
- ⁶C. J. Stevenson and J. Peakall, "Effects of topography on lofting gravity flows: Implications for the deposition of deep-water massive sands," *Mar. Pet. Geol.* **27**, 1366 (2010).
- ⁷M. R. Oshaghi, H. Afshin, and B. Firoozabadi, "Experimental investigation of the effect of obstacles on the behavior of turbidity currents," *Can. J. Civ. Eng.* **40**, 343 (2013).
- ⁸S. A. Asghari Pari, S. M. M. Kashfipour, and M. Ghomeshi, "An experimental study to determine the obstacle height required for the control of subcritical and supercritical gravity currents," *Eur. J. Environ. Civ. Eng.* (published online).
- ⁹J. H. Jung and H. S. Yoon, "Effect of scour depth on flow around circular cylinder in gravity current," *Ocean Eng.* **117**, 78, doi:10.1016/j.oceaneng.2016.03.025 (2016).
- ¹⁰E. Meiburg and B. Kneller, "Turbidity currents and their deposits," *Annu. Rev. Fluid Mech.* **42**, 135 (2010).
- ¹¹C. H. Pilskalns, J. H. Churchill, and L. M. Mayer, "Resuspension of sediment by bottom trawling in the Gulf of Maine and potential geochemical consequences," *Conserv. Biol.* **12**, 1223 (1998).
- ¹²H. E. Huppert, "The propagation of two-dimensional and axisymmetric viscous gravity currents over a rigid horizontal surface," *J. Fluid Mech.* **121**, 43 (1982).
- ¹³J. W. Rottman and J. E. Simpson, "Gravity currents produced by instantaneous releases of a heavy fluid in a rectangular channel," *J. Fluid Mech.* **135**, 95 (1983).
- ¹⁴B. Kneller and C. Buckee, "The structure and fluid mechanics of turbidity currents: A review of some recent studies and their geological implications," *Sedimentology* **47**, 62 (2000).
- ¹⁵G. V. Middleton, "Sediment deposition from turbidity currents," *Annu. Rev. Earth Planet. Sci.* **21**, 89 (1993).
- ¹⁶M. R. Jacobson and F. Y. Testik, "Turbulent entrainment into fluid mud gravity currents," *Environ. Fluid Mech.* **14**, 541 (2014).
- ¹⁷B. R. Morton, G. Taylor, and J. S. Turner, "Turbulent gravitational convection from maintained and instantaneous sources," *Proc. R. Soc. A* **234**, 1 (1956).
- ¹⁸T. H. Ellison and J. S. Turner, "Turbulent entrainment in stratified flows," *J. Fluid Mech.* **6**, 423 (1959).
- ¹⁹J. S. Turner, "Turbulent entrainment: The development of the entrainment assumption, and its application to geophysical flows," *J. Fluid Mech.* **173**, 431 (1986).
- ²⁰H. J. S. Fernando, "Turbulent mixing in stratified fluids," *Annu. Rev. Fluid Mech.* **23**, 455 (1991).
- ²¹R. L. Fernandez and J. Imberger, "Bed roughness induced entrainment in a high Richardson number underflow," *J. Hydraul. Res.* **44**, 725 (2006).
- ²²C. Cenedese and C. Adduce, "Mixing in a density-driven current flowing down a slope in a rotating fluid," *J. Fluid Mech.* **604**, 369 (2008).
- ²³O. E. Sequeiros, "Estimating turbidity current conditions from channel morphology: A Froude number approach," *J. Geophys. Res.: Oceans* **117**, C04003, doi:10.1029/2011jc007201 (2012).
- ²⁴H. I. S. Nogueira, C. Adduce, E. Alves, and M. J. Franca, "Dynamics of the head of gravity currents," *Environ. Fluid Mech.* **14**, 519 (2014).
- ²⁵V. Lombardi, C. Adduce, G. Sciortino, and M. La Rocca, "Gravity currents flowing upslope: Laboratory experiments and shallow-water simulations," *Phys. Fluids* **27**, 016602 (2015).
- ²⁶L. Ottolenghi, C. Adduce, R. Inghilesi, F. Roman, and V. Armenio, "Mixing in lock-release gravity currents propagating up a slope," *Phys. Fluids* **28**, 056604 (2016).
- ²⁷C. Cenedese, J. A. Whitehead, T. A. Ascarelli, and M. Ohiwa, "A dense current flowing down a sloping bottom in a rotating fluid," *J. Phys. Oceanogr.* **34**, 188, doi:10.1175/1520-0485(2004)034<0188:adcfda>2.0.co;2 (2004).
- ²⁸R. I. Wilson, *Optimisation of Lighting Techniques for Photometric Measurement of Sediment-Laden Flows* (IAHR, The Hague, The Netherlands, 2015).
- ²⁹J. W. Rottman, J. E. Simpson, J. C. R. Hunt, and R. E. Britter, "Unsteady gravity current flows over obstacles: Some observations and analysis related to the phase II trials," *J. Hazard. Mater.* **11**, 325 (1985).
- ³⁰E. Gonzalez-Juez and E. Meiburg, "Shallow-water analysis of gravity-current flows past isolated obstacles," *J. Fluid Mech.* **635**, 415 (2009).
- ³¹T. Tokyay and G. Constantinescu, "The effects of a submerged non-erodible triangular obstacle on bottom propagating gravity currents," *Phys. Fluids* **27**, 056601 (2015).
- ³²G. F. Lane-Serff, L. M. Beal, and T. D. Hadfield, "Gravity current flow over obstacles," *J. Fluid Mech.* **292**, 39 (1995).
- ³³J. Hacker, P. F. Linden, and S. B. Dalziel, "Mixing in lock-release gravity currents," *Dyn. Atmos. Oceans* **24**, 183, doi:10.1016/0377-0265(95)00443-2 (1996).
- ³⁴M. R. Jacobson and F. Y. Testik, "On the concentration structure of high-concentration constant-volume fluid mud gravity currents," *Phys. Fluids* **25**, 016602 (2013).
- ³⁵M. A. Hallworth, H. E. Huppert, J. C. Phillips, and R. S. J. Sparks, "Entrainment into two-dimensional and axisymmetric turbulent gravity currents," *J. Fluid Mech.* **308**, 289 (1996).
- ³⁶M. A. Hallworth, J. C. Phillips, H. E. Huppert, and R. S. J. Sparks, "Entrainment in turbulent gravity currents," *Nature* **362**, 829 (1993).
- ³⁷M. Princevac, H. J. S. Fernando, and C. D. Whiteman, "Turbulent entrainment into natural gravity-driven flows," *J. Fluid Mech.* **533**, 259 (2005).
- ³⁸C. Adduce, G. Sciortino, and S. Proietti, "Gravity currents produced by lock exchanges: Experiments and simulations with a two-layer shallow-water model with entrainment," *J. Hydraul. Eng.* **138**, 111 (2012).